ACS OMEGA

http://pubs.acs.org/journal/acsodf

Article

# Network Basis for the Heat-Adapted Structural Thermostability of Bacterial Class II Fructose Bisphosphate Aldolase

Guangyu Wang*

Cite This: *ACS Omega* 2023, 8, 17731−17739

Read Online

ACCESS | Metrics & More | Article Recommendations

**ABSTRACT:** The sufficient structural thermostability of a biological macromolecule is an overriding need for green nanoreactors and nanofactories to secure high activity. However, little is still known about what specific structural motif is responsible for it. Here, graph theory was employed to examine if the temperature-dependent noncovalent interactions and metal bridges, as identified in the structures of *Escherichia coli* class II fructose 1,6-bisphosphate aldolase, could shape a systematic fluidic grid-like mesh network with topological grids to regulate the structural thermostability of the wild-type construct and its evolved variants in each generation upon decyclization. The results indicated that the biggest grids may govern the temperature thresholds for their tertiary structural perturbations but without affecting the catalytic activities. Moreover, lower grid-based systematic thermal instability may facilitate structural thermostability, but a highly independent thermostable grid may still be required to serve as a critical anchor to secure the stereospecific thermoactivity. Its end melting temperature thresholds, together with the start ones of the biggest grids in the evolved variants, may confer high temperature sensitivity against thermal inactivation. Collectively, this computational study may have widespread significance in advancing our complete understanding and biotechnology of the thermoadaptive mechanism of the structural thermostability of a biological macromolecule.

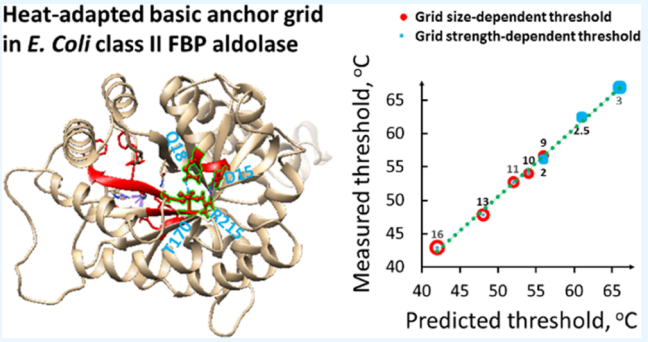


## INTRODUCTION

The activity of a biological macromolecule is based on its structural thermostability, which is generally controlled by a melting temperature threshold ($T_m$) at which the secondary structure starts unfolding. Nonetheless, the point mutation-based evolution can weaken the tertiary structural thermostability, causing thermal inactivation of the relevant activity. A well-known example is the deletion of F508 in the cystic fibrosis transmembrane conductance regulator (CFTR), which results in the most popular cystic fibrosis.[1−5] On the other hand, the evolution by family DNA shuffling and random mutagenesis also allows the suppressor point mutation to enhance the structural thermostability in favor of the higher activity at elevated temperatures.[6,7] A good example is *Escherichia coli* (*E. coli*) or *Edwardsiella ictaluri* (*E. ictaluri*) class II fructose 1,6-bisphosphate (FBP) aldolase, which employs a bimetallic-binding site to catalyze the reversible aldol condensation of dihydroxyacetone phosphate (DHAP) and glyceraldehyde-3-phosphate (G3P) to make FBP along the glycolytic pathway.[8] Although both parental wild-type (WT) metal-dependent enzymes were rapidly inactivated at temperatures above 48 °C and had no stereospecific activity at 55 °C, variants from four generations between two shuffled bacterial enzymes can increase the systematic thermostability so that both the start and end temperature thresholds for the enzyme activity are raised by about 10 °C, but the catalytic function is not influenced at room temperature.[8,9]

Despite the available high-resolution crystal structures of this ligand-free *E. coli* class II FBP aldolase,[10,11] the structural factors or motifs for the heat-adapted thermostability are still missing until a DNA hairpin thermal biosensor was reported in 2013.[12] It employs the different loop sizes or H-bonds in the stem to tune the initial structural melting temperature ($T_m$) as a critical functional threshold ($T_{th}$) and thereafter to monitor a change in the environmental temperature with high sensitivity. Generally, the smaller hairpin size and the more H-bonds in the stem facilitate a higher $T_m$ and $T_{th}$.[12] Since both a single DNA hairpin and a grid in a grid-like noncovalent interaction mesh network in the enzyme share a common topological circle in general terms and the dissociation of this network grid by heat is analogous to

Received: January 23, 2023
Accepted: April 28, 2023
Published: May 11, 2023





https://doi.org/10.1021/acsomega.3c00473
*ACS Omega* 2023, 8, 17731−17739

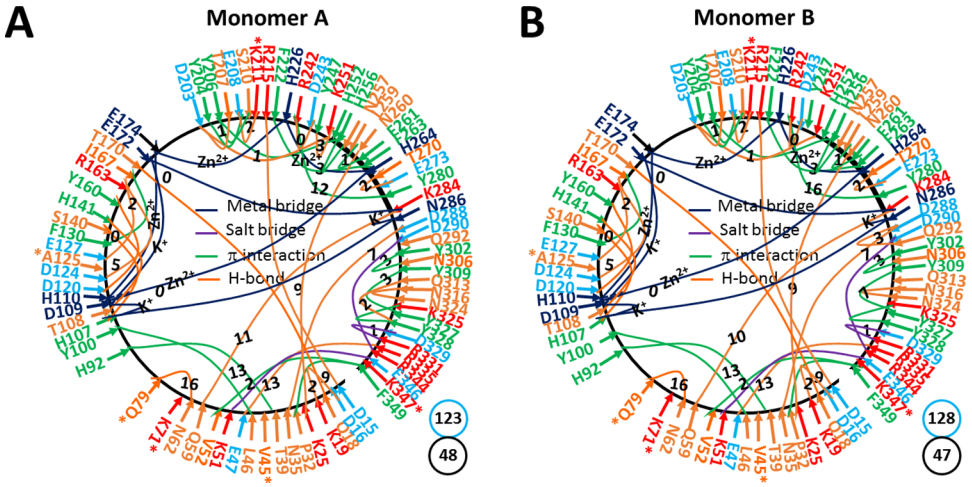


**Figure 1.** Topological grids in the systemic fluidic grid-like noncovalently interacting mesh network along the single polypeptide chain of the ligand-free WT class II *E. coli* FBP aldolase dimer at 293 K. The X-ray crystallographic structures of monomers A (A) and B (B) in WT class II *E. coli* FBP aldolase at 293 K (PDB ID, 1DOS) were used for the model. Salt bridges, metal bridges, $\pi$-interactions, and H-bonds between pairing amino acid side chains along the single polypeptide chain from D15 to F349 are marked in purple, dark blue, green, and orange, respectively. The grid sizes required to control the relevant noncovalent interactions and metal bridges were calculated with graph theory and are labeled in black. The total grid sizes and grid size-controlled noncovalent interactions and metal bridges along the single polypeptide chain are shown in the blue and black circles, respectively.

DNA hairpin melting, it is exciting to hypothesize that WT class II *E. coli* FBP aldolase and its evolved variants exploit a fluidic system of temperature-dependent grid-like noncovalently interacting mesh networks with topological grids to keep the three-dimensional (3D) structures of this bacterial enzyme for the different thermoadaptive structural stabilities.

In this *in silico* study, graph theory was used to examine the hypothesis by carefully decoding each grid in the respective grid-like noncovalently interacting mesh networks as identified in the crystal structures of WT class II *E. coli* FBP aldolase at 293 K.[10] Two equations based on the findings of the DNA hairpin thermal detector were also developed to assess the melting temperature threshold ($T_m$) of the biggest grid and grid-based systematic thermal instability ($T_i$) so that the structural factors or motifs for the heat-adapted structural thermostability against thermal inactivation could be revealed and discussed.

The melting temperature threshold of the DNA hairpin thermosensor above 34 °C can be raised by 20 °C with the H-bonded G−C base pairs doubled or the loop length diminished from 20 to 10 As.[12] Thereby, a grid size ($S$) and grid size-governed equivalent H-bonds in the network grid may be important for the melting temperature threshold. In this *in silico* study, after the grid size was defined and calculated by graph theory as the minimal number of the total side chains of residues in the protein that did not engage in any noncovalent interactions and metal bridges in a grid, the biggest grid along the single polypeptide chain could then be screened and identified. For the biggest grid to carry out the single-rate-limiting-step melting reaction like DNA hairpins in favor of a change in the tertiary structures in the bacterial enzyme and its variants, the calculated melting temperature threshold ($T_m$) of the biggest grid should be comparable to the experimental threshold ($T_{th}$).

On the other hand, in light of smaller loops or more H-bonds in the stem favoring the higher thermostability of a DNA hairpin,[12] the systematic grid-like noncovalent interaction mesh network along the single polypeptide chain can reorganize along with the melting of the biggest grid. Accordingly, after the systemic thermal instability ($T_i$) was also defined and calculated as a ratio of the total grid sizes to the total noncovalent interactions and metal bridges along the same single polypeptide chain, this new parameter could render an important energetic reference for the heat-adapted structural thermostability.

Following those two newly defined parameters, the traditional temperature coefficient or sensitivity ($Q_{10}$, the ratio of the activities of an enzyme for 10 °C intervals) of the thermostability-dependent thermal inactivation was also analyzed and discussed.

Taken as a whole, it was amazing to find that the systematic thermal instability of this bacterial enzyme was significantly decreased by the one-by-one suppressor mutation during several generations, along with the increased start and end melting temperature thresholds, which were matched theoretically and experimentally very well with high sensitivity.[8] Of special note, an independent, stable, and thermoadaptive anchor grid is very important to secure a dynamic active site of proteins including enzymes. Therefore, this novel grid thermodynamic model may be useful to predict the melting temperature thresholds precisely for the thermoadaptive structural thermostability of a biological macromolecule once the accurate 3D structure is determined. The precise and successful prediction may, in turn, stimulate broad scientific and commercial applications.

## MATERIALS AND METHODS

**Data Mining Resources.** In this computational study, the X-ray crystallographic structures of the class II *E. coli* fructose 1,6-bisphosphate aldolase dimer at 293 K in the presence of $(NH_4)_2SO_4$ (PDB ID, 1DOS, model resolution = 1.6 Å) were analyzed with graph theory to uncover the roles of the biggest grids with minimal sizes and strengths in regulating the melting temperature threshold ($T_m$) parameters for their heat-adapted thermostability.[10]

**Standards for Noncovalent Interactions.** In order to secure results to be reproduced with high sensitivity, the same standard definition as described previously,[13,14] together with structure visualization software, UCSF Chimera, was exploited to identify stereo- or regioselective interdomain diagonal and intradomain lateral noncovalent interactions in WT class II *E.*


https://doi.org/10.1021/acsomega.3c00473
ACS Omega 2023, 8, 17731−17739

*coli* FBP aldolase at 293 K and to examine their potential roles in shaping topological grids with minimal sizes to govern the $T_m$ for the changes in the tertiary structures of the WT enzyme and the evolved variants in each generation and related $T_i$ values. Those noncovalent interactions included salt bridges, cation/CH/lone pair/$\pi-\pi$ interactions, and H-bonds along the single polypeptide chain from D15 to F349.

**Preparation of Topological Grid Maps by Using Graph Theory.** Once noncovalent interactions were scanned along the single polypeptide chain from D15 to F349, a grid was then defined by graph theory as the smallest topological circle with a minimal size to stabilize a noncovalent interaction in it. The whole grids with minimal sizes were geometrically mapped for class II *E. coli* FBP aldolase at 293 K. A black line represented the initial amino acid sequence from D15 to F349. Each vertex ($v$) represented a single amino acid side chain involving a noncovalent interaction or a metal bridge along the single polypeptide chain and was marked with an arrow in different colors. Each edge represented a noncovalent interaction or a metal bridge between two vertices in a biochemical network and was marked in the same color for the same kind of interaction, otherwise in a different one. A topological grid was shaped between two vertices, $i$ and $j$ ($v_i$ and $v_j$), if and only if there was a path from $v_i$ to $v_j$ and a return path from $v_j$ to $v_i$. The grid size ($S$) was then defined as the minimal number of the total side chains of residues that did not engage in any noncovalent interaction or metal bridge in a grid. For a given grid-like biochemical reaction mesh network, the grid size between $v_i$ and $v_j$ was the total shortest return path distance from vertex $j$ to $i$ as the direct shortest path distance from vertex $i$ to $j$ was zero once there was a noncovalent interaction or a metal bridge between them. Here, the Floyd−Warshall algorithm was exploited to calculate the shortest return path between the two vertices $i$ and $j$ ($v_i$ and $v_j$).[15] For example, in the biochemical reaction network of Figure 1A, a direct path length from N62 and Q79 is zero because of an H-bond between them. However, another shortest return path existed from Q79 to N62 in this grid. Since the sum of residues, $^{63}$GGASFIAGKGVKSDVP$^{78}$ (Figure 3),[10] which did not involve any noncovalent interaction in the grid, was 16, the grid size was 16. Once each noncovalent interaction, together with metal bridges, was tracked by a controlled grid size and the uncommon sizes were marked in black, a grid with an $x$-residue size in monomer A or B was denoted as Grid$_{x\text{-A}}$ or Grid$_{x\text{-B}}$, respectively. If the same size was involved in several grids, $n$ was also, in turn, inserted as Grid$_{x\text{-}n\text{-A}}$ or Grid$_{x\text{-}n\text{-B}}$. Taken together, the total noncovalent interactions and metal bridges and the total grid sizes along the single polypeptide chain were shown in black and blue circles beside the mesh network map for the calculation of the systematic thermal instability.

**Equations.** When a noncovalent interaction in the grid is broken at a temperature, that temperature is defined as a melting threshold ($T_{th}$). If both a DNA hairpin and the biggest grid melt in a similar manner and the melting is rate-limiting for the thermal inactivation, the $T_{th}$ for the changes in the thermostability of proteins was calculated from the $T_m$ of the biggest grid along the single polypeptide chain using the following equation, as described previously[13,14]

$$T_m\ (^\circ\mathrm{C}) = 34 + (n-2) \times 10 + (20 - S_{max}) \times 2 \quad (1)$$

where $n$ is the total number of the H-bonds equivalent to noncovalent interactions in the biggest grid and $S_{max}$ is the size of the biggest grid.

In either state, the grid-based systemic thermal instability ($T_i$) along the single polypeptide chain was defined using the following equation, as described previously[13,14]

$$T_i = S/N \quad (2)$$

where $S$ is the total grid sizes along the single polypeptide chain of one subunit in a functional state and $N$ is the total noncovalent interactions and metal bridges along the same single polypeptide chain of one subunit in the same functional state.

The temperature coefficient ($Q_{10}$) of the thermal inactivation of this bacterial enzyme was calculated using the following equation:

$$Q_{10} = -(X_1/X_2)^{10/(T_2-T_1)} \quad (3)$$

where $X_1$ and $X_2$ are the relative activities obtained at temperatures $T_1$ and $T_2$ (measured in Kelvin), respectively.

## RESULTS

**Native Class II *E. coli* FBP Aldolase Dimer at 293 K Had the Overall Nonidentical Twin Grid Structures.** Monomers A and B from the same primary sequence in the ligand-free WT class II *E. coli* FBP aldolase dimer are paired as twins.[10] The dimeric interface had the H99-L84′, W293-Y328′, W296-W333′, and Y303-Y303′ swapping $\pi$-interactions.[10] In each subunit, H110, E174, H226, and H264 formed common $Zn^{2+}$ bridges, leading to the smallest grid with a zero-residue size. Similarly, H107, D109, E172, K284, and N286 are connected together via $K^+$ to generate another smallest common grid with a zero-residue size.[10] In addition, the following noncovalent interactions were shared by both monomers along the single polypeptide chain from D15 to F349 (Figure 1).

First, three salt bridges were found between several charged pairs. They included K51-E346, D290-R344, and D329-R331 (Figure 1).

Second, fifteen $\pi$-interactions were present between aromatic residues and nearby residues. For example, $\pi$-interacting pairs had P32-F349-V52, T39-H92, L46-Y100, F130-I167, Y204-E208, Y206-S210/H252, F222-F263, R242-Y280, H256-N257, L259-F261, Y302-N306, Y309-Y327, and K325-Y328 (Figure 1).

Third, nineteen H-bonds were observed between a variety of hydrophilic residues. The H-bonding pairs included D15-R215, D16-K19, Q18-T170, K25-N260, N35-D288, E47-R335, Q59-K284, N62-Q79, H107-S140, T108-H141, D120-Y160, D124/E127-R163, D203-T207/K251, E208-K211, R242-D243, T270-E273, and N316-N324 (Figure 1).

On the other hand, there were some different noncovalent interactions between amino acid side chains in the two subunits.[10] For example, the Y247-K251 and Q313-Y328 H-bonds were present in monomer A but absent in monomer B. In contrast, a D288-Q292 H-bond in monomer B was not shown in monomer A (Figure 1). These differences brought about different total noncovalent interactions together with metal bridges and total grid sizes as 48 and 123 for monomer A and 47 and 128 for monomer B, respectively. Thus, the systematic thermal instability ($T_i$) values were 2.56 and 2.72 for monomers A and B of the WT construct, respectively (Tables 1 and 2). In addition, despite those differences, the grid size ranges were the same from 0 to 16 in monomers A and B (Figure 1).

**K211A Mutation in the Evolved Variant 1-37D6 Did Not Change the Biggest Grid Size and the Related Start Melting Temperature Threshold Range in the First**



https://doi.org/10.1021/acsomega.3c00473
ACS Omega 2023, 8, 17731−17739

**Table 1. Critical Suppressor Point Mutations Introduced in the Thermostable Class II Bacterial FBP Aldolases during Four Evolved Generations**

| residue position | 45 | 71 | 79 | 82 | 211 | 347 |
|---|---|---|---|---|---|---|
| WT *E. coli* FBP aldolase | V | K | Q | A | K | K |
| WT *E. ictaluri* FBP aldolase | V | K | Q | | A | Q |
| 1-37D6 | V | K | Q | | A | K |
| 1-44F2 | V | K | L | | A | K |
| 2-15B2 | A | K | L | | A | K |
| 3-4C10 | A | K | L | | A | R |
| 4-4C10 | A | K | L | | A | R |
| 4-43D6 | A | I | L | | V | R |
| 4-4C10/K71I | A | I | L | | A | R |
| 4-4C10//K211V | A | K | L | | V | R |

**Generation.** In the first generation, the K211A mutation was found along with the deletion of A82 in the evolved variant 1-37D6 of class II *E. coli* FBP aldolase (Table 1).[8] Figure 1 shows that the deletion of A82 did not affect any noncovalent interaction (Figure 1). However, the K211A mutation disrupted two grids. In monomer A, one was $Grid_2$ with a 2-residue size via the shortest path from K211 to E208; the other was $Grid_{12}$ with a 12-residue size via the shortest path from D15 to Q18, T170, E172, K284, Y280, R242, D243, Y247, K251, D203, Y204, E208, K211, and R215 and back to D15 (Figure 2). In monomer B, the broken Y247-K251 H-bond increased the grid size from 12 to 16 (Figure 2). When these grids were broken, the biggest $Grid_{16\text{-}1A}$ in monomer A and $Grid_{16\text{-}2B}$ in monomer B were still maintained (Figure 1). Both grids had a 16-residue size via the shortest path from N62 to Q79 and back to N62 (Figure 3). Therefore, the calculated start $T_m$ values were 42 °C when two equivalent H-bonds sealed $Grid_{16\text{-}1A}$ and $Grid_{16\text{-}2B}$ (Figure 3 and Tables 1 and 2). This value was not affected by the K211A mutation, so the whole start melting temperature thresholds should be 42 °C (Tables 1 and 2). In consonance with this prediction, the measured start $T_{th}$ value for thermal inactivation is about 43.0 °C (Tables 1 and 2).[8] Of special note, the K211A mutation reduced the total noncovalent interactions and metal bridges to 46 and 45 and the total grid sizes to 109 and 110 residues for monomers A and B, respectively. Hence, the systematic thermal instability ($T_i$) values decreased to 2.37 and 2.44 for monomers A and B, respectively (Tables 1 and 2).

**Q79A Mutation in the Evolved Variant 1-44F2 Increased the Calculated Start Melting Temperature Threshold in the First Generation.** Following the K211A mutation, the Q79L mutation was observed in the evolved variant 1-44F2.[8] Such a mutation disconnected the N62-Q79 H-bond and related $Grid_{16\text{-}1A}$ in monomer A and $Grid_{16\text{-}2B}$ in monomer B (Figure 3). In this case, both the biggest grids had a common 13-residue size via the shortest path from T39 to L46, Y100, and H92 and back to T39 (Figure 1). When the L46-Y100 and H92-T39 $\pi$-interactions sealed the common grid, the calculated start $T_m$ was 48 °C (Tables 1 and 2). Thus, it was reasonable that the evolved variant 1-44F2 had a measured $T_{th}$ 47.9 °C to start thermal inactivation (Tables 1 and 2).[8]

Once the N62-Q79 H-bond was disrupted, the total grid sizes and the total noncovalent interactions and metal bridges were further diminished to 93 and 45 for monomers A and 94 and 44 for monomer B, respectively (Figure 1 and Tables 1 and 2). In this regard, the systematic thermal instability ($T_i$) values were further lowered to 2.07 for monomer A and 2.14 for monomer B, respectively (Tables 1 and 2).

**V45A Mutation in the Evolved Variant 2-15B2 Further Increased the Calculated Start Melting Temperature Thresholds in the Second Generation.** Based on the K211A and Q79L mutations in the first generation, V45 was further mutated to alanine in the evolved variant 2-15B2 during the second generation. When this mutation disrupted the L46-Y100 and H92-T39 $\pi$-interactions in $Grid_{13\text{-}1A}$ and $Grid_{13\text{-}1B}$ (Figure 4), the first biggest $Grid_{13\text{-}2A}$ in monomer A and $Grid_{13\text{-}2B}$ in monomer B had 2.5 equivalent H-bonds to produce a start $T_m$ value as 53 °C (Figure 5 and Tables 1 and 2). Meanwhile, the second biggest $Grid_{11\text{-}A}$ in monomer A and $Grid_{10\text{-}B}$ in monomer B with 2.0 equivalent H-bonds had start $T_m$ values of 52 and 54 °C, respectively (Figure 5 and Tables 1 and 2). Hence, in direct line with these predicted values, the measured start $T_{th}$ value was 52.8 °C (Tables 1 and 2).[8]

On the other hand, along with the broken L46-Y100 and H92-T39 $\pi$-interactions in $Grid_{13\text{-}1A}$ and $Grid_{13\text{-}1B}$, the total grid sizes and the total noncovalent interactions and metal bridges were further decreased to 80 and 43 for monomer A and 81 and 42 for

**Table 2. Grid Thermodynamic Model-Based New Parameters of WT Class II Bacterial FBP Aldolase and the Evolved Variants in Each Generation**

| construct | monomer | grid # | $S_{max}$, a.a | equivalent H-bonds for $S_{max}$ | calculated start $T_m$, °C | measured start $T_{th}$, °C | $S$ | $N$ | $T_i$ |
|---|---|---|---|---|---|---|---|---|---|
| WT *E. coli* FBP aldolase | A | 16-1A | 16 | 2 | 42 | 43 | 123 | 48 | 2.56 |
| | B | 16-1B 16-2B | 16 | 2 | 42 | 43 | 128 | 47 | 2.72 |
| WT *E. ictaluri* FBP aldolase | A | 16-1A | 16 | 2 | 42 | 43 | 109 | 46 | 2.37 |
| | B | 16-2B | 16 | 2 | 42 | 43 | 110 | 45 | 2.44 |
| 1-37D6 | A | 16-1A | 16 | 2 | 42 | 43 | 109 | 46 | 2.37 |
| | B | 16-2B | 16 | 2 | 42 | 43 | 110 | 45 | 2.44 |
| 1-44F2 | A | 13-1A | 13 | 2 | 48 | 47.9 | 93 | 45 | 2.07 |
| | B | 13-1B | 13 | 2 | 48 | 47.9 | 94 | 44 | 2.14 |
| 2-15B2 | A | 11-A 13-2A | 11, 13 | 2, 2.5 | 52−53 | 52.8 | 80 | 43 | 1.86 |
| | B | 10-B 13-2B | 10, 13 | 2, 2.5 | 53−54 | 52.8 | 81 | 42 | 1.93 |
| 3-4C10 | A | 9-1A | 9 | 2 | 56 | 56.8 | 56 | 41 | 1.37 |
| | B | 9-1B | 9 | 2 | 56 | 56.8 | 58 | 40 | 1.45 |
| 4-4C10 | A | 9-1A | 9 | 2 | 56 | 54.9 | 56 | 41 | 1.37 |
| | B | 9-1B | 9 | 2 | 56 | 54.9 | 58 | 40 | 1.45 |
| 4-43D6 | A | 9-1A | 9 | 2 | 56 | 56.8 | 56 | 41 | 1.37 |
| | B | 9-1B | 9 | 2 | 56 | 56.8 | 58 | 40 | 1.45 |



https://doi.org/10.1021/acsomega.3c00473
ACS Omega 2023, 8, 17731−17739

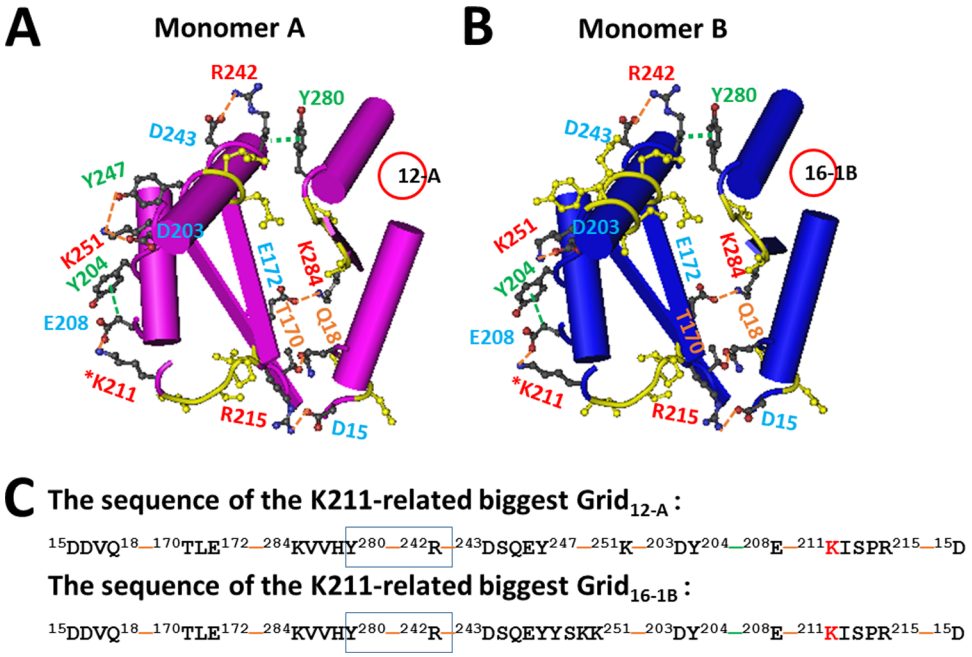


**Figure 2.** Structures of the K211-related biggest grids in the systemic fluidic grid-like mesh network of the ligand-free WT class II *E. coli* FBP aldolase dimer at 293 K. (A) Structure of $Grid_{12\text{-}A}$ in monomer A. (B) Structure of $Grid_{16\text{-}1B}$ in monomer B. The grid size $S_{max}$ is shown as the first number in a red circle. (C) Sequences of the K211-related biggest $Grid_{12\text{-}A}$ and $Grid_{16\text{-}1B}$ to control the R242-Y280 $\pi$-interactions in blue boxes.

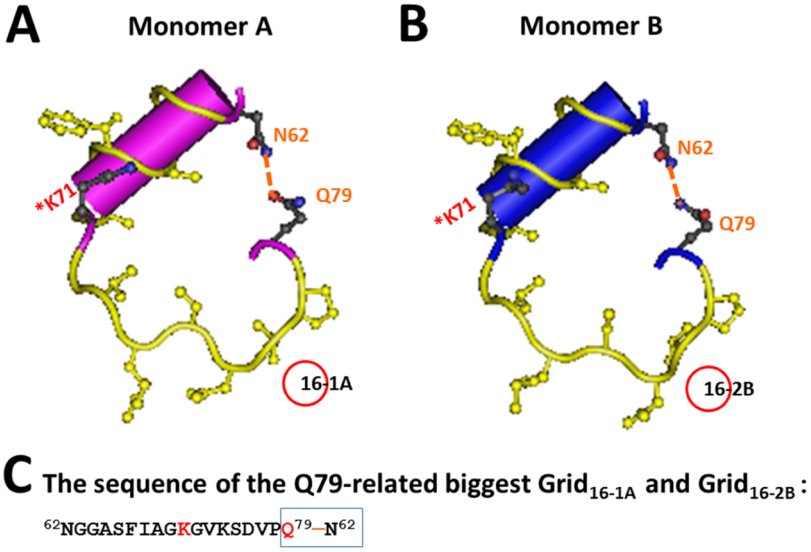


**Figure 3.** Structures of the Q79-related biggest grids in the systemic fluidic grid-like mesh network of the ligand-free WT class II *E. coli* FBP aldolase dimer at 293 K. (A) Structure of $Grid_{16\text{-}1A}$ in monomer A. (B) Structure of $Grid_{16\text{-}2B}$ in monomer B. The grid size $S_{max}$ is shown as the first number in a red circle. (C) Sequence of the Q79-related biggest $Grid_{16\text{-}1A}$ and $Grid_{16\text{-}2B}$ to control the N62-Q79 H-bonds in blue boxes.

monomer B, respectively (Figure 1 and Tables 1 and 2). Thus, the systematic thermal instability ($T_i$) values further declined to 1.86 for monomer A and 1.93 for monomer B (Tables 1 and 2).

**K347R Mutation in the Evolved Variants 3-4C10, 4-4C10, and 4-43D6 Further Increased the Calculated Start Melting Temperature Thresholds in the Third and Fourth Generations.** $Grid_{13\text{-}2A}$ in monomer A and $Grid_{13\text{-}2B}$ had a common 13-residue size via the shortest path from E47 to K51, E346, and R335 and back to E47. Meanwhile, $Grid_{11\text{-}A}$ in monomer A had an 11-residue size via the shortest path from K51 to Q59, K284, N286, D290, R344, and E346 and back to K51; $Grid_{10\text{-}B}$ in monomer B had a 10-residue size via the similar shortest path from K51 to E346 but with a D288-Q292 H-bond to shorten the return path to 10 (Figure 5). Because these grids involved K347, the key mutation K347R in the evolved variants 3-4C10, 4-4C10, and 4-43D6 during the third and fourth generations may interact with nearby E346 and thus disrupt both strong E47-R335 and Q59-K284 H-bonds in these grids.[8] In this case, $Grid_{9\text{-}1A}$ in monomer A and $Grid_{9\text{-}1B}$ in monomer B became sensitive to elevated temperature (Figure 6). As both had a 9-residue size via the shortest path from K25 to Q18, T170, E172, D109, H110, H264, F261, L259, and N260 and back to K25 to control two H-bonds between Q18 and T170 and between K25 and N260, the calculated start $T_m$ was about 56 °C, which was close to the measured start $T_{th}$ values 54.9 °C


https://doi.org/10.1021/acsomega.3c00473
ACS Omega 2023, 8, 17731−17739

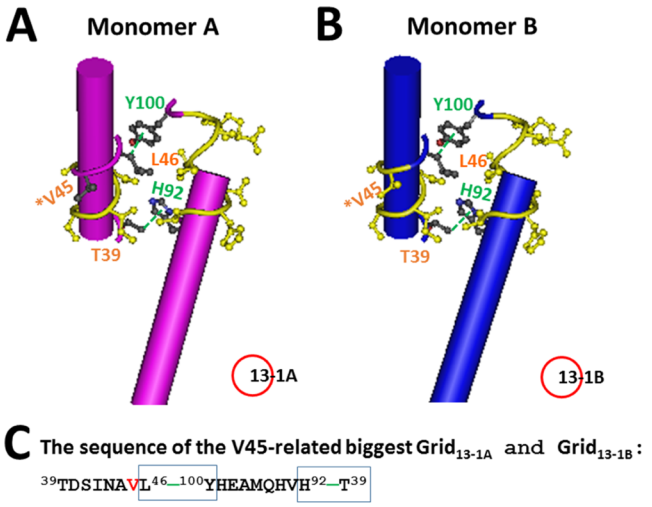


**Figure 4.** Structures of the V45-related biggest grids in the systemic fluidic grid-like mesh network of the ligand-free WT class II *E. coli* FBP aldolase dimer at 293 K. (A) Structure of $Grid_{13\text{-}1A}$ in monomer A. (B) Structure of $Grid_{13\text{-}1B}$ in monomer B. The grid size $S_{max}$ is shown as the first number in a red circle. (C) Sequence of the V45-related biggest $Grid_{13\text{-}1A}$ and $Grid_{13\text{-}1B}$ to control the L46-Y100 and T39-H92 $\pi$-interactions in blue boxes.

for thermal inactivation in the variant 4-4C10 and 56.8 °C in the variants 3-4C10 and 4-43D6 (Figure 6 and Tables 1 and 2).[8]

Following the broken E47-R335 H-bonds in $Grid_{13\text{-}3A}$ and $Grid_{13\text{-}2B}$ and the disrupted Q59-K284 H-bonds in $Grid_{11\text{-}A}$ and $Grid_{10\text{-}B}$, the total grid sizes and the total noncovalent interactions and metal bridges were further decreased to 56 and 41 for monomer A and 58 and 40 for monomer B, respectively. Thereby, the systematic thermal instability ($T_i$) values were inherently weakened to 1.37 and 1.45 for monomers A and B, respectively (Tables 1 and 2).[8]

**$Grid_{9\text{-}2A}$ in Monomer A and $Grid_{9\text{-}2B}$ in Monomer B Served as Basic Anchors for the Heat-Adapted Structural Thermostability.** Once the Q18-T170 and K25-N260 H-bonds in $Grid_{9\text{-}1A}$ and $Grid_{9\text{-}1B}$ were broken above the predicted 56 °C, $Grid_{9\text{-}2A}$ and $Grid_{9\text{-}2B}$ were, in turn, sensitive to higher temperatures. They also exhibited a 9-residue size via the shortest path from D15 to Q18, T170, E172, D109, H110, H264, F263, F222, and R215 and back to D15 to control the Q18-T170 and D15-R215 H-bonds (Figure 6). However, D15 also formed an additional salt bridge with R215. Therefore, once the total 3.0 equivalent H-bonds sealed the grids, a common calculated $T_m$ was about 66 °C, which was near the experimental end threshold of 66.9 °C for thermal inactivation in both variants 4-4C10 and 4-43D6 (Figure 6 and Tables 1 and 3).[8] Thus, $Grid_{9\text{-}2A}$ and $Grid_{9\text{-}2B}$ may serve as basic anchors to secure the catalytic activity of the enzyme by stabilizing the metal-dependent enzyme structure. Once this anchor is dissociated, the systematic thermal instability ($T_i$), even if may be still low, would not make sense for the heat-adapted structural thermostability against thermal inactivation.

## DISCUSSION

Heat- or cold-adapted structural thermostability of a biological macromolecule is very important not only for life to keep functionally active over a wide range of environmental temperatures in each organism but also for durable industrial biocatalysts and multitasking synthetic chemistry. However, not all of the macromolecules including proteins have had their tertiary structures captured at more than one temperature, and hence it is still a challenge to predict the effect of temperature on their conformations without any priori information except for the high-resolution 3D structure. Recently, a graph theory-based grid thermodynamic model has been successfully employed to predict the melting temperature thresholds for the changes in the specific tertiary and secondary structures and in the specific functional activity of class I aldolase B.[14] In this case study, graph theory was further used as a structure-based *ab initio* approach independently to investigate what structural factors control the heat-adapted structural thermostability of two model glycolytic enzymes, *E coli* and *E. ictaluri* class II FBP aldolases, and the evolved variants in each generation against thermal inactivation.

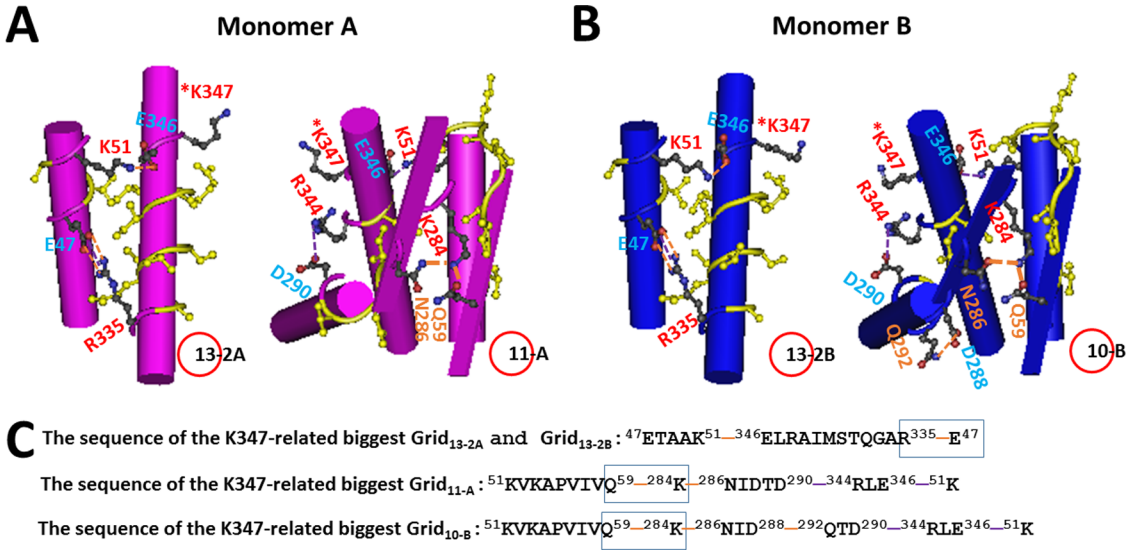


**Figure 5.** Structures of the K347-related biggest grids in the systemic fluidic grid-like mesh network of the ligand-free WT class II *E. coli* FBP aldolase dimer at 293 K. (A) Structures of $Grid_{13\text{-}2A}$ and $Grid_{11\text{-}A}$ in monomer A. (B) Structures of $Grid_{13\text{-}2B}$ and $Grid_{10\text{-}B}$ in monomer B. The grid size $S_{max}$ is shown as the first number in a red circle. (C) Sequences of the K347-related biggest $Grid_{13\text{-}2A}$ and $Grid_{13\text{-}2B}$ to control the E47-R335 H-bonds and $Grid_{11\text{-}A}$ and $Grid_{10\text{-}B}$ to control the Q59-K284 H-bonds in blue boxes.



https://doi.org/10.1021/acsomega.3c00473
ACS Omega 2023, 8, 17731−17739

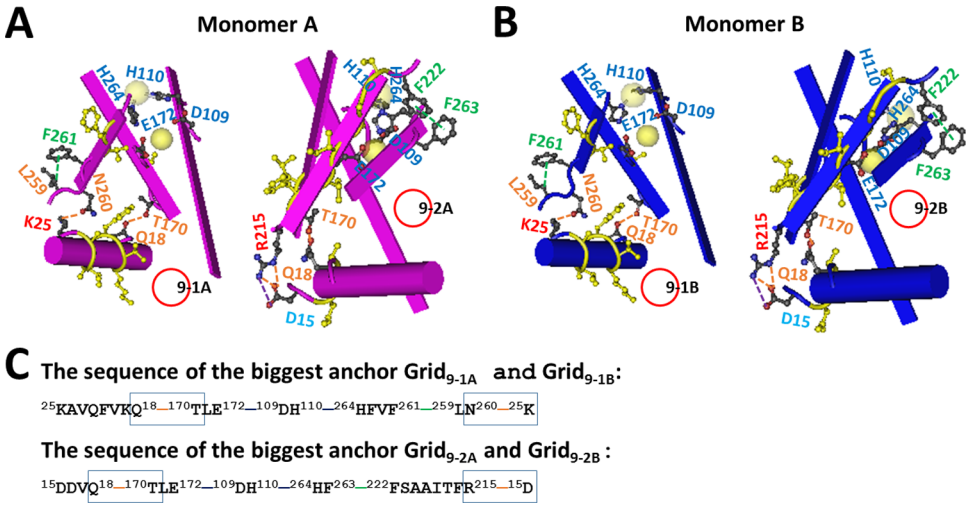


**Figure 6.** Structures of the biggest anchor grids in the systemic fluidic grid-like mesh network of the ligand-free WT class II *E. coli* FBP aldolase dimer at 293 K. (A) Structures of $Grid_{9\text{-}1A}$ and $Grid_{9\text{-}2A}$ in monomer A. (B) Structures of $Grid_{9\text{-}1B}$ and $Grid_{9\text{-}2B}$ in monomer B. The grid size $S_{max}$ is shown as the first number in a red circle. Two yellow spheres are two metal ions. (C) Sequences of the biggest anchor $Grid_{9\text{-}1A}$ and $Grid_{9\text{-}1B}$ to control the K25-N260 and Q18-T170 H-bonds and $Grid_{9\text{-}2A}$ and $Grid_{9\text{-}2B}$ to control the D15-R215 and Q18-T170 H-bonds in blue boxes.

**Table 3. End Melting Temperature Threshold for Thermal Inactivation of WT Bacterial Class II FBP Aldolase and the Evolved Variants in Each Generation**

| construct | monomer | grid # | $S_{max}$, a.a | equivalent H-bonds for $S_{max}$ | calculated end $T_m$, °C | measured end $T_{th}$, °C |
|---|---|---|---|---|---|---|
| WT *E.coli* FBP aldolase | A | 9-2A | 9 | 2 | 56 | 55.0 |
| | B | 9-2B | 9 | 2 | 56 | 55.0 |
| WT *Ed. ictaluri* FBP aldolase | A | 9-2A | 9 | 2 | 56 | 55.0 |
| | B | 9-2B | 9 | 2 | 56 | 55.0 |
| 1-37D6 | A | 9-2A | 9 | 2 | 56 | 57.9 |
| | B | 9-2B | 9 | 2 | 56 | 57.9 |
| 1-44F2 | A | 9-2A | 9 | 2 | 56 | 58.8 |
| | B | 9-2B | 9 | 2 | 56 | 58.8 |
| 2-15B2 | A | 9-2A | 9 | 2.5 | 61 | 61.9 |
| | B | 9-2B | 9 | 2.5 | 61 | 61.9 |
| 3-4C10 | A | 9-2A | 9 | 2.5 | 61 | 63.0 |
| | B | 9-2B | 9 | 2.5 | 61 | 63.0 |
| 4-4C10 | A | 9-2A | 9 | 3 | 66 | 66.9 |
| | B | 9-2B | 9 | 3 | 66 | 66.9 |
| 4-43D6 | A | 9-2A | 9 | 3 | 66 | 66.9 |
| | B | 9-2B | 9 | 3 | 66 | 66.9 |

The results demonstrated that the melting temperature threshold of the biggest grid in the grid-like noncovalently interacting mesh network along the single polypeptide chain may determine a start threshold for a change in the structural thermostability, while the melting temperature threshold of the basic anchor grid in the same network system may control the end threshold for the thermostability during thermal inactivation. Although the systematic thermal instability ($T_i$) declined with the increased start and end melting temperature thresholds, the combined thresholds with a small interval in each generation still maintained a high-temperature sensitivity ($Q_{10}$) for the thermal inactivation.

For WT *E coli* and *E. ictaluri* class II FBP aldolases, the biggest $Grid_{16\text{-}1B}$ and $Grid_{16\text{-}2B}$ in monomer B had a common calculated start $T_m$ as 42 °C (Figures 1−3 and Tables 1 and 2), which was consistent with the measured start $T_{th}$ 43 °C for those two WT constructs (Tables 1 and 2).[8] When the R242-Y280 $\pi$-interaction in $Grid_{16\text{-}1B}$ and N62-Q79 H-bonds in $Grid_{16\text{-}2B}$ and $Grid_{16\text{-}1A}$ were broken above 42 °C, the basic anchor $Grid_{9\text{-}2A}$ in monomer A and $Grid_{9\text{-}2B}$ in monomer B may have 2.0 equivalent H-bonds to seal both grids so that they would have a common calculated 56 °C as an end $T_m$. This value was in agreement with the measured end $T_{th}$ 55.0 °C (Figure 6 and Tables 1−3).[8]

For the evolved variant 1-37D6 in the first generation, the biggest $Grid_{16\text{-}1A}$ in monomer A and $Grid_{16\text{-}2B}$ in monomer B had the predicted start $T_m$ 42 °C (Figure 3 and Tables 1 and 2), which was similar to the experimental start $T_{th}$ 43 °C (Tables 1 and 2).[8] When N62-Q79 H-bonds were disrupted above 43 °C, the basic anchor $Grid_{9\text{-}2A}$ and $Grid_{9\text{-}2B}$ may still have 2.0 equivalent H-bonds for a predicted 56 °C as an end $T_m$, which was also near the measured end $T_{th}$ 57.9 °C (Figure 6 and Tables 1−3).[8]

For the evolved variant 1-44F2 in the first generation, the calculated start $T_m$ of both $Grid_{13\text{-}1A}$ and $Grid_{13\text{-}1B}$ was 48 °C (Figure 4 and Tables 1 and 2), which was near the measured start $T_{th}$ 47.9 °C (Tables 1 and 2).[8] With the L46-Y100 and H92-T39 $\pi$-interactions in $Grid_{13\text{-}1A}$ and $Grid_{13\text{-}1B}$ disconnected, the basic anchor $Grid_{9\text{-}2A}$ and $Grid_{9\text{-}2B}$ may still allow at least 2 equivalent H-bonds to have a predicted end $T_m$ 56 °C, which


https://doi.org/10.1021/acsomega.3c00473
ACS Omega 2023, 8, 17731−17739

was similar to the measured $T_{th}$ 58.8 °C (Figure 6 and Tables 1−3).[8]

For the evolved variant 2-15B2 in the second generation, the biggest $Grid_{11\text{-}A}$ and $Grid_{13\text{-}2A}$ in monomer A generated a calculated start $T_m$ range from 52 to 53 °C (Figure 5 and Tables 1 and 2). On the other hand, the biggest $Grid_{10\text{-}B}$ and $Grid_{13\text{-}2B}$ in monomer B created a calculated start $T_m$ range from 53 to 54 °C (Figure 5 and Tables 1 and 2). Therefore, the average start $T_m$ was about 53 °C (Figure 5 and Tables 1 and 2), which was also in accordance with the measured $T_{th}$ 52.8 °C (Tables 1 and 2).[8] Upon the disruption of the E47-R335 H-bonds in $Grid_{13\text{-}2A}$ and $Grid_{13\text{-}2B}$ and the Q59-K284 H-bonds in $Grid_{11\text{-}A}$ and $Grid_{10\text{-}B}$ above 53 °C, the number of the equivalent H-bonds in the basic anchors $Grid_{9\text{-}2A}$ and $Grid_{9\text{-}2B}$ may also increase to 2.5 so that the calculated end $T_m$ was about 61 °C (Tables 1−3), which approximated the measured end $T_{th}$ 61.9 °C (Figure 6 and Tables 1−3).[8]

For other evolved variants 3-4C10, 4-4C10, and 4-43D6 during the third and fourth generations, the calculated start common $T_m$ of $Grid_{9\text{-}1A}$ and $Grid_{9\text{-}1B}$ was about 56 °C, which was similar to the measured start $T_{th}$ from 54.9 to 56.8 °C. When the K25-N260 H-bond was disconnected, the remaining $Grid_{9\text{-}2A}$ and $Grid_{9\text{-}2B}$ may still have at least 2.5 equivalent H-bonds so that the calculated end $T_m$ was about 61 °C, which was comparable to the end $T_{th}$ 63 °C for the variant 3-4C10 (Figure 6 and Tables 1−3).[8] However, for 4-4C10 and 4-43D6, the equivalent H-bonds in $Grid_{9\text{-}2A}$ and $Grid_{9\text{-}2B}$ may be increased up to 3 so that the calculated end $T_{th}$ would be about 66 °C, which was in line with the measured end $T_{th}$ 66.9 °C (Figure 6 and Tables 1−3).[8] Because rotamer simulations between Q16 and T170 and between D15 and R215 demonstrated that the maximal equivalent H-bonds were 3.5, the maximal end $T_{th}$ limit may be 71 °C (Figure 6).

When K71 was reinstated in the presence of the K211V mutation in variant 4-4C10, the biggest $Grid_{13\text{-}1A}$ and $Grid_{13\text{-}1B}$ with a 13-residue size via the shortest path from T39 to L46, Y100, and H92 and back to T39 may allow a lower calculated start $T_m$ 48 °C (Figure 4 and Tables 1 and 2), which was near the calculated start $T_m$ of 48 °C in the evolved variant 1-44F2 (Tables 1 and 2). Therefore, that may be why the measured $T_{1/2}$ for thermal inactivation was back to 51.4 °C.[8]

It is interesting that the systematic thermal instability ($T_i$) of the bacterial metalloenzyme decreased from 2.56 to 1.37 in monomer A and from 2.72 to 1.45 in monomer B during four generations (Tables 1 and 2). This decreasing trend was consistent with the increases in the calculated start $T_m$ values from 42 to 56 °C and the measured start $T_{th}$ values from 43 to 56.8 °C (Tables 1 and 2), and the calculated end $T_m$ values from 56 to 66 °C and the measured end $T_{th}$ values from 55.0 to 66.9 °C (Tables 1−3). Further studies are necessary to define the temperature range of the rational and precise design along with the prediction of thermoadaptive enzyme activity on the grounds of graph theory and the grid thermodynamic model. The enzymes include but are not limited to other class II fructose 1,6-bisphosphate aldolases.

Finally, the thermal inactivation curves of purified WT *E. coli* and *E. ictaluri* class II FBP aldolases and most of the evolved variants exhibited a high-temperature sensitivity ($Q_{10}$) for thermal inactivation in a range from −47.0 to −92.1.[8] Such a high $Q_{10}$ may be achieved by the small intervals between start and end melting temperature thresholds (Tables 1−3). For example, when the relative activity of WT class II *E. coli* FBP aldolase declined from 0.9 to 0.1, the corresponding temperature increased by 5 °C. Therefore, $Q_{10}$ was −81. Of special note, when the H-bonds $Grid_{9\text{-}1A}$ and $Grid_{9\text{-}1B}$ and $Grid_{9\text{-}2A}$ and $Grid_{9\text{-}2B}$ were broken from K25-N260 to shared Q18-T170 and then to D15-R215, for the most stable variant 4-43D6, $Q_{10}$ was about −88.6. Therefore, an independent and stable basic anchor is the overriding need to secure a dynamic active site in proteins including enzymes against thermal inactivation.

Generally speaking, molecular dynamics simulations can link the global thermal movements from the corresponding starting structure at room temperature to catalysis and the unfolding region so as to illuminate the thermoadaptive mechanisms of enzymes.[16,17] However, in this special computational study, two groups of strong metal bridges coupled the stable basic anchor $Grid_{9\text{-}2A}$ or $Grid_{9\text{-}2B}$ with the prior biggest grids from $Grid_{16\text{-}1A}$ and $Grid_{16\text{-}2B}$ to $Grid_{11\text{-}A}$ and $Grid_{10\text{-}B}$ together to secure the long-term local structural stability against thermal inactivation (Figures 1−6). Therefore, those biggest grids could function as a series of heat fuses to be melted one by one independently upon elevated temperatures but without a global conformational change to affect the catalytic activity of the enzyme.[8] Therefore, the thermodynamic molecular simulations may be unnecessary.

## CONCLUSIONS

This computational study has mechanistically related the crystallographic static conformation to the biochemical findings on detailed atomic scales, conferring a creative and insightful bioinformatics solution. With regard to the start and end melting temperature thresholds of the bacterial class II FBP aldolases and the evolved variants during generations, the successful theoretical and experimental comparisons demonstrated that once the systematic fluidic grid-like mesh network of non-covalent interactions and metal bridges are available, graph theory can be used to establish a powerful grid thermodynamic model for the rational and precise prediction and design of durable thermoadaptive structural stability of proteins including enzymes, thereby meeting the increasing needs for promising robust biocatalytic applications and stereo-, regio-, or enantioselective synthetic chemistry in biotechnology, food, and pharmaceutical industries.

## ASSOCIATED CONTENT

### Data Availability Statement

All data generated or analyzed during this study are included in this published article.

## AUTHOR INFORMATION

### Corresponding Author

**Guangyu Wang** − *Department of Physiology and Membrane Biology, University of California School of Medicine, Davis, California 95616, United States;* Present Address: Department of Drug Research and Development, Institute of Biophysical Medico-chemistry, Reno, NV 89523, U.S.A; orcid.org/0000-0002-5581-6926; Email: gary.wang10@gmail.com, gyuwang@ucdavis.edu

Complete contact information is available at: https://pubs.acs.org/10.1021/acsomega.3c00473

### Author Contributions

G.W. wrote the main manuscript text, prepared Table 1−3 and Figures 1−6, and reviewed the whole manuscript.

### Notes

The author declares no competing financial interest.



https://doi.org/10.1021/acsomega.3c00473
*ACS Omega* 2023, 8, 17731−17739

## ■ ACKNOWLEDGMENTS

The author's own studies cited in this article were supported by an NIDDK grant (DK45880 to D.C.D.), a Cystic Fibrosis Foundation grant (DAWSON0210), an NIDDK grant (2R56DK056796-10), and an American Heart Association (AHA) grant (10SDG4120011 to GW).

## ■ CONVENTIONS AND ABBREVIATIONS

CFTR, cystic fibrosis transmembrane conductance regulator; DHAP, dihydroxyacetone phosphate; FBP, fructose 1,6-bisphosphate; G3P, glyceraldehyde-3-phosphate; $T_m$, melting temperature; $T_{th}$, temperature threshold; WT, wild type

## ■ REFERENCES

(1) Aleksandrov, A. A.; Kota, P.; Cui, L.; Jensen, T.; Alekseev, A. E.; Reyes, S.; He, L.; Gentzsch, M.; Aleksandrov, L. A.; Dokholyan, N. V.; Riordan, J. R. Allosteric modulation balances thermodynamic stability and restores function of deltaF508 CFTR. *J. Mol. Biol.* **2012**, *419*, 41−60.

(2) Liu, X.; O'Donnell, N.; Landstrom, A.; Skach, W. R.; Dawson, D. C. Thermal instability of ΔF508 CFTR channels function: protection by single suppressor mutations and inhibiting channel activity. *Biochemistry* **2012**, *51*, 5113−5124.

(3) Wang, G. Interplay between inhibitory ferric and stimulatory curcumin regulates phosphorylation-dependent human cystic fibrosis transmembrane conductance regulator and ΔF508 activity. *Biochemistry* **2015**, *54*, 1558−1566.

(4) Wang, G. Molecular basis for Fe(III)-independent curcumin potentiation of cystic fibrosis transmembrane conductance regulator activity. *Biochemistry* **2015**, *54*, 2828−2840.

(5) Wang, G.; Linsley, R.; Norimatsu, Y. External $Zn^{2+}$ binding to cysteine-substituted cystic fibrosis transmembrane conductance regulator constructs regulates channel gating and curcumin potentiation. *FEBS J.* **2016**, *283*, 2458−2475.

(6) Crameri, A.; Raillard, S. A.; Bermudez, E.; Stemmer, W. P. C. DNA shuffling of a family of genes from diverse species accelerates directed evolution. *Nature* **1998**, *391*, 288−291.

(7) Moore, G. L.; Maranas, C. D. Modeling DNA mutation and recombination for directed evolution experiments. *J. Theor. Biol.* **2000**, *205*, 483−503.

(8) Hao, J.; Berry, A. A thermostable variant of fructose bisphosphate aldolase constructed by directed evolution also shows increased stability in organic solvents. *Protein Eng., Des. Sel.* **2004**, *17*, 689−697.

(9) Jacques, B.; Coinc, M.; Sygusch, J. Active site remodeling during the catalytic cycle in metal-dependent fructose-1,6-bisphosphate aldolases. *J. Biol. Chem.* **2018**, *293*, 7737−7753.

(10) Blom, N. S.; Tetreault, S.; Coulombe, R.; Sygusch, J. Novel active site in *Escherichia Coli* fructose 1,6-biophosphate aldolase. *Nat. Struct. Mol. Biol.* **1996**, *3*, 856−862.

(11) Cooper, S. J.; Leonard, G. A.; McSweeney, S. M.; Thompson, A. W.; Naismith, J. H.; Qamar, S.; Plater, A.; Berry, A.; Hunter, W. N. The crystal structure of a class II fructose-1,6-bisphosphate aldolase shows a novel binuclear metal-binding active site embedded in a familiar fold. *Structure* **1996**, *4*, 1303−1315.

(12) Jonstrup, A. T.; Fredsøe, J.; Andersen, A. H. DNA hairpins as temperature switches, thermometers and ionic detectors. *Sensors* **2013**, *13*, 5937−5944.

(13) Wang, G.Graphic insights into the network basis for heat-gated TRPV1 *BioRxiv*, 2022 DOI: 10.1101/2022.01.02.474701.

(14) Wang, G.The Network Basis for the Structural Thermostability and the Functional Thermoactivity of Aldolase B *BioRxiv*, 2022 DOI: 10.1101/2022.10.20.513014. Wang, G. The Network Basis for the Structural Thermostability and the Functional Thermoactivity of Aldolase B. *Molecules.* **2023**, *28*, No. 1850.

(15) Floyd, R. W. Algorithm-97 - Shortest Path. *Commun. ACM* **1962**, *5*, 345.

(16) Vieille, C.; Zeikus, G. J. Hyperthermophilic enzymes: sources, uses, and molecular mechanisms for thermostability. *Microbiol. Mol. Biol. Rev.* **2001**, *65*, 1−43.

(17) Dick, M.; Weiergräber, O. H.; Classen, T.; Bisterfeld, C.; Bramski, J.; Gohlke, H.; Pietruszka, J. Trading off stability against activity in extremophilic aldolases. *Sci. Rep.* **2016**, *6*, No. 17908.



https://doi.org/10.1021/acsomega.3c00473
*ACS Omega* 2023, 8, 17731−17739